Surface-Wave Pulse Routing around Sharp Right Angles

Z. Gao,[1] H. Xu,[1] F. Gao,[1,4] Y. Zhang,[1] Y. Luo,[2,*] and B. Zhang[1,3,†]

[1]*Division of Physics and Applied Physics, School of Physical and Mathematical Sciences, Nanyang Technological University, Singapore 637371, Singapore*

[2]*School of Electrical and Electronic Engineering, Nanyang Technological University, Nanyang Avenue, Singapore 639798, Singapore*

[3]*Centre for Disruptive Photonic Technologies, Nanyang Technological University, Singapore 637371, Singapore*

[4]*State Key Laboratory of Modern Optical Instrumentation, Zhejiang University, Hangzhou 310027, China*

(Received 25 July 2017; revised manuscript received 13 December 2017; published 16 April 2018)

Surface-plasmon polaritons (SPPs), or localized electromagnetic surface waves propagating on a metal-dielectric interface, are deemed promising information carriers for future subwavelength terahertz and optical photonic circuitry. However, surface waves fundamentally suffer from scattering loss when encountering sharp corners in routing and interconnection of photonic signals. Previous approaches enabling scattering-free surface-wave guidance around sharp corners are limited to either volumetric waveguide environments or extremely narrow bandwidth, being unable to guide a surface-wave pulse (SPP wave packet) on an on-chip platform. Here, in a surface-wave band-gap crystal implemented on a single metal surface, we demonstrate in time-domain routing a surface-wave pulse around multiple sharp right angles without perceptible scattering. Our work not only offers a solution to on-chip surface-wave pulse routing along an arbitrary path, but it also provides spatiotemporal information on the interplay between surface-wave pulses and sharp corners, both of which are desirable in developing high-performance large-scale integrated photonic circuits.

DOI: 10.1103/PhysRevApplied.9.044019

I. INTRODUCTION

Surface-plasmon polaritons (SPPs) generally described as electromagnetic (EM) surface waves on a metal-dielectric interface [1] show promising potential to merge photonics and electronics on the same metal circuitry [2,3] because of their inherent subwavelength confinement. Although metals are remarkably lossy in the visible spectrum and beyond, they can be treated as perfect electric conductors with negligible loss in the far-infrared, terahertz, and microwave spectra. Spoof SPPs are EM surface modes at these frequency bands, supported on a periodically textured metal surface [4,5]. They show great potential in building high-efficiency subwavelength photonic circuits and other unprecedented functional devices from microwave to infrared spectra [6–13]. However, while being routine in electronic circuits, near-perfect transmission through sharp right angles is fundamentally difficult for (spoof) SPP waveguides because of the intrinsic scattering loss of guiding EM surface waves around sharp corners. The scattered energy will not only deteriorate transmission, but it also introduces unwanted cross talk of signals being especially detrimental in compactly integrated photonic circuits.

To date, scattering-free guidance of EM surface waves around sharp corners has been realized only in photonic topological insulators [14–18], which support topological EM surface states as an analogue of electronic chiral edge states in topological insulators and later in surface-wave transformation cloaks [19], which apply transformation optics to effectively warp the EM space around sharp corners analogous to the way in which gravity curves space in general relativity. However, these approaches generally require a volumetric waveguide environment (usually between two parallel metal plates) to achieve the out-of-plane confinement or apply only to a very narrow bandwidth being unable to manipulate surface-wave pulses (SPP wave packets) on a single metal surface.

Nevertheless, the capability of manipulating surface-wave pulses is extremely desirable in ultrafast optical data processing and recording [20–23]. It is, therefore, necessary to have a clearer and more complete understanding of the spatiotemporal interplay between surface-wave pulses and the underlying photonic structures carrying them. The surface-wave pulse propagation at optical frequencies has been directly imaged along a straight path using the

*To whom correspondence should be addressed. luoyu@ntu.edu.sg

†To whom correspondence should be addressed. blzhang@ntu.edu.sg

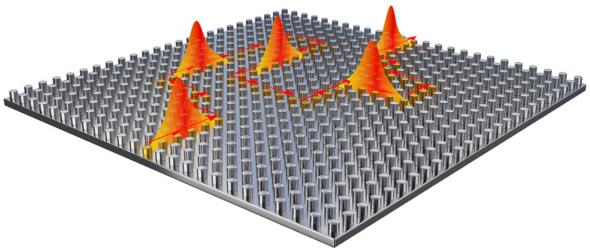

FIG. 1. Schematic of a surface-wave pulse routing through multiple sharp right angles along a tortuous path in a surface-wave band-gap crystal.

femtosecond-laser-pulse tracking technique [24–28]. However, how a surface-wave pulse interacts with a sharp corner remains unobserved in reality, not to mention the imaging of the process of routing a surface-wave pulse around sharp corners with near-perfect transmission.

It is the purpose of this article to develop an approach of routing surface-wave pulses around multiple sharp right angles, especially with the spatiotemporal information on the routing process. We first show that by introducing a line defect in a photonic band-gap crystal for surface waves, the surface waves can be tightly guided along the line defect in the surface-wave band gap [29–30]. Then, by tracking and mapping a surface-wave pulse as it propagates around multiple sharp right angles in a surface-wave band-gap crystal, as schematically shown in Fig. 1, we demonstrate that near-perfect transmission around multiple sharp right angles can be achieved for surface-wave pulses. Note that similar concepts of a photonic band gap for surface-plasmon modes [31] and waveguiding in SPP band-gap structures [32] have been reported in the visible frequency regime where the metal surface supports real SPPs.

The remarkable high-efficiency time-domain surface-wave pulse routing around multiple sharp right angles in the surface-wave band-gap crystals is mainly because of the following two reasons. First, the wide forbidden band gap of the surface-wave band-gap crystal suppresses scattering of surface waves into the ambient space in a broad bandwidth. This feature is similar to previous wavelength-scale photonic circuits in a photonic crystal [33–35]. Second, because the eigenmode supported by each rod in the line-defect waveguide is essentially a coupled toroidal resonance mode and an electric quadrupole mode with fourfold rotational symmetry [36–38] (more details are discussed later), the near-field couplings between the rod at the corner of the right-angle bend and its two immediate neighbors before and after the right-angle bend are the same. Therefore, the guided waves are deceived as if they are still propagating along a straight waveguide. This mechanism for high-efficiency transmission through sharp bends originates from Yariv's coupled-resonator optical waveguide (CROW) theory [39]. There is no need to purposely construct extra local resonances [40,41] at the corner in order to facilitate tunneling the EM energy through, being in sharp contrast to previous photonic-crystal-based proposals [33–35].

II. EXPERIMENTAL DEMONSTRATION OF THE SURFACE-WAVE BAND GAP

We start the experimental demonstration with a surface-wave band-gap crystal that consists of a periodic (period $d = 5.0$ mm) 25×25 square lattice of circular metal rods with height $H = 5.0$ mm and radius $r = 1.25$ mm, all standing on a flat metallic surface, as shown in Fig. 2(a). The calculated band structure, as shown in Fig. 2(b), reveals a complete forbidden band gap for surface waves from 12.6 to 27 GHz for the current surface-wave band-gap crystal. Using a vector network analyzer (Agilent Technologies N5225A) and two homemade monopole antennas placed at two opposite sides of the experimental sample, we measure the continuous-wave transmission spectrum supported by the surface-wave band-gap crystal, as shown in Fig. 2(c). The measured transmission exhibits a substantial drop from 12.6 to 27 GHz, corresponding to the forbidden band gap of the surface-wave band-gap crystal.

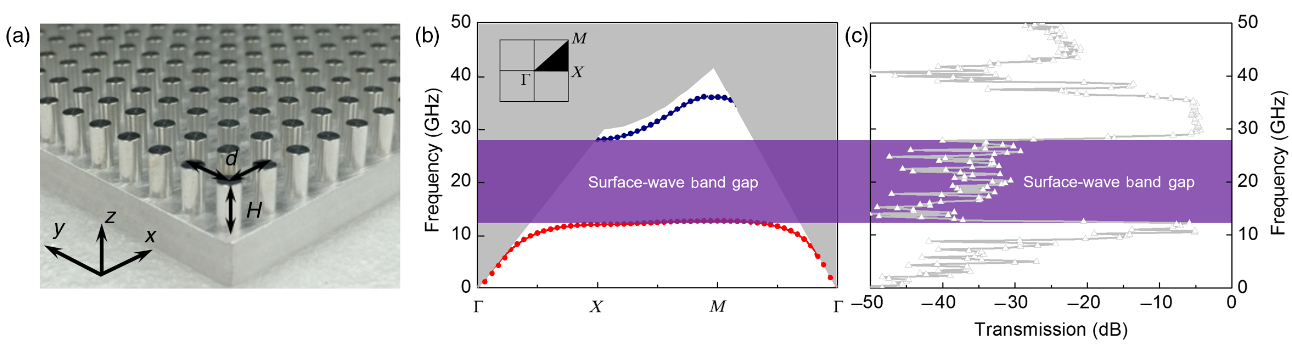

FIG. 2. Experimental demonstration of a surface-wave band-gap crystal. (a) Photograph of the surface-wave band-gap crystal. A square array of aluminum rods (with height $H = 5$ mm and periodicity $d = 5$ mm) stand on a metallic surface. (b) Calculated band structure of the surface-wave band-gap crystal. Purple region represents the forbidden band gap. (c) Measured transmission spectrum through the surface-wave band-gap crystal.

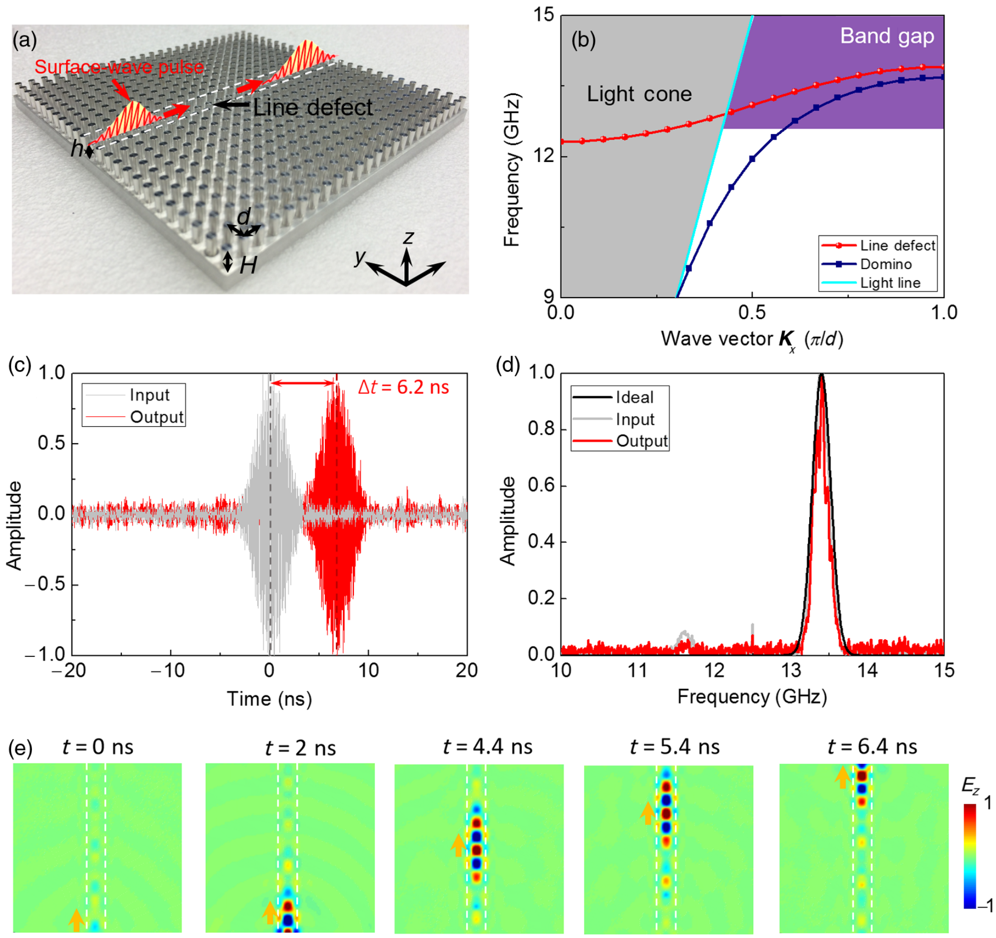

FIG. 3. Surface-wave pulse propagation along a straight-line-defect waveguide. (a) Photograph of the straight-line-defect waveguide formed by shortening a row of metallic rods from $H = 5$ mm to $h = 4.3$ mm in the middle of the surface-wave band-gap crystal with a schematic of the pulse propagation superimposed. (b) Dispersion of the line-defect waveguide compared to that of the traditional domino-plasmon waveguide. Purple region represents the forbidden band gap of the surface-wave band-gap crystal. (c) Measured surface-wave pulse signals at the input and output of the waveguide. Hz (d) Spectral signatures of the measured input pulse and output pulse compared with the ideal case. (e) Reconstructed surface-wave pulse propagation in the straight-line-defect waveguide at different time frames.

III. TIME-DOMAIN SURFACE-WAVE PULSE PROPAGATION ALONG A STRAIGHT-LINE-DEFECT WAVEGUIDE

A straight line defect can be constructed by shortening the height of a row of rods in the middle from $H = 5.0$ mm to $h = 4.3$ mm, as indicated in Fig. 3(a). Figure 3(b) shows the dispersion (red line) of the line-defect waveguide that is calculated with the eigenmode solver of the commercial software CST Microwave Studio (see more details in the Method section of the Supplemental Material [42]). Note that only the part below the light line and within the band gap (purple region) can confine and guide surface waves along the line-defect waveguide.

In fact, even without the surrounding surface-wave band-gap crystal, this row of shortened rods themselves can also guide surface waves. This is a typical traditional surface-wave waveguide (widely referred to as "domino plasmons" [8]) that has been studied extensively with various device applications [10,43–49]. For comparison, we also simulate the dispersion [blue line in Fig. 3(b)] of surface waves guided along this domino-plasmon waveguide when all the other rods of the surrounding surface-wave band-gap crystal are removed. It can be seen that this domino-plasmon waveguide exhibits a polaritonic dispersion that starts from the light line and then tends to zero group velocity at the Brillouin zone edge.

We use an arbitrary waveform generator (Tektronix AWG70001A) to generate an 800-MHz-wide Gaussian pulse centered around 13.4 GHz within the line-defect waveguiding band and launch it into the line-defect waveguide through an input monopole antenna. Using another output monopole antenna connected to an oscilloscope (Tektronix MSO 72004C), we measure the pulse signal at the third rod from the input as the input pulse [gray line in Fig. 3(c); delay time 0 ns] in order to minimize the interference from the source. Similarly, the output pulse [red line in Fig. 3(c)] is measured at the third rod from the output in order to avoid the interference from the end of the line-defect waveguide and is normalized by the maximum amplitude of the measured input pulse. Note that since we cannot completely absorb the output pulse at the end of the waveguide, there is slight reflection due to the impedance mismatch between the waveguide output and the surrounding air environment. As shown in Fig. 3(c), it takes 6.2 ns for the pulse to propagate through the 100-mm-long straight-line-defect waveguide.

Figure 3(d) shows the spectral signature of the measured pulse signal. For comparison, the ideal pulse profile as the input to the arbitrary waveform generator is also shown. As the surface-wave pulse propagates along the straight-line-defect waveguide, it maintains its amplitude and spectral signature without perceptible distortion.

In the following, we reconstruct the dynamic images of pulse propagation based on the microwave near-field imaging measurement. Two steps are adopted in the experiment. First, we map the surface-wave near-field distributions (electric field component E_z) on a transverse plane 1 mm above the line-defect waveguide, covering the frequency range from 13 to 13.8 GHz with a step of 0.01 GHz (the spectral measurement and near-field imaging results are shown in Fig. S1 in the Supplemental Material [42]). Second, we reconstruct the original surface-wave pulse by using the measured surface-wave near-field distributions with different frequencies (see more details in the Method section of the Supplemental Material [42]).

Figure 3(e) shows the reconstructed images of surface-wave pulse propagation through the line-defect waveguide. The pulse signal reaches the last rod at 6.4 ns, being consistent with the measured time delay of 6.2 ns in Fig. 3(c). Video S1 (see the video in the Supplemental Material [42]) shows more details of the propagating pulse along the straight-line-defect waveguide.

IV. TIME-DOMAIN SURFACE-WAVE PULSE PROPAGATION ALONG A U-SHAPED LINE-DEFECT WAVEGUIDE

We then examine the performance of a U-shaped line-defect waveguide with two right-angle sharp corners [Fig. 4(a)]. Using the same experimental method as in Fig. 3, we measure the input pulse and the output pulse, which are shown in Fig. 4(b). The measured two pulse signals are almost the same after the pulse propagates through two right-angle sharp corners.

We reconstruct the images of dynamic pulse propagation from the measured near-field distributions (the spectral measurement and near-field imaging results are shown in Fig. S2 of the Supplemental Material [42]). The reconstructed images are shown in Fig. 4(c). It can be seen that the pulse reaches the first and second right-angle corners at 4 and 6 ns, respectively. The pulse is guided around both corners, leaving the U-shaped line-defect waveguide at 8 ns with imperceptible scattering. Video S2 (see the video in the Supplemental Material [42]) displays the whole process of the pulse propagation through the U-shaped line-defect waveguide.

For comparison, we also reconstruct the surface-wave pulse propagation along a U-shaped domino-plasmon waveguide, when all the other rods in the surrounding surface-wave band-gap crystal are removed. As presented in Fig. 4(d), the pulse reaches the first sharp corner at 1.4 ns and the second sharp corner at 2 ns. Both corners cause strong scattering and reflection, leading to almost zero transmission at the output. Video S3 (see the video in the Supplemental Material [42]) shows more details about the process of the pulse through the U-shaped domino-plasmon waveguide.

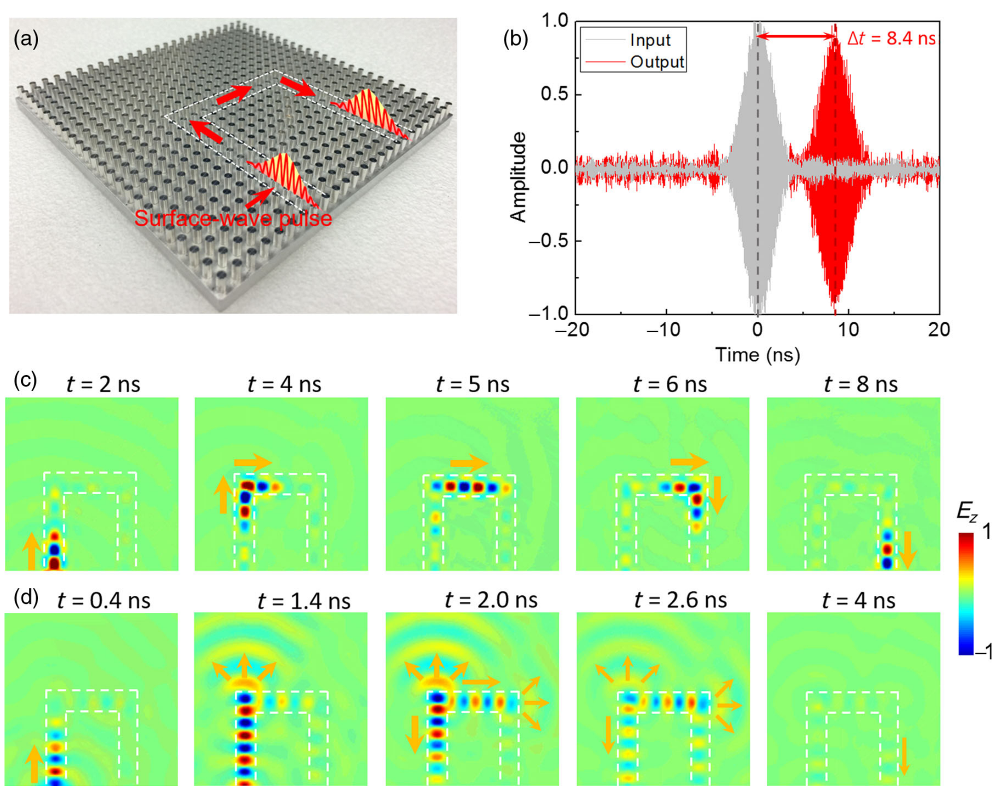

FIG. 4. Surface-wave pulse propagation around a U-shaped line-defect waveguide with two sharp right angles. (a) Photograph of the U-shaped line-defect waveguide with a schematic of the pulse propagation superimposed. (b) Measured surface-wave pulse at the input and output of the U-shaped line-defect waveguide. (c) Reconstructed surface-wave pulse propagation in the U-shaped line-defect waveguide at different time frames. (d) Reconstructed surface-wave pulse propagation in the U-shaped domino-plasmon waveguide at different time frames.

V. MECHANISM OF SURFACE-WAVE PULSE GUIDANCE AROUND SHARP RIGHT ANGLES

To understand the underlying mechanism of the high-efficiency surface-wave pulse guidance around a sharp right angle, we first simulate the magnetic and electric field distributions of an isolated point defect that can be realized by shortening only one single rod (black circle) in the surface-wave band-gap crystal, as shown in Figs. 5(a) and 5(d), in which a transverse plane at the half height of the 5-mm-high metallic rods is adopted. The closed loop of magnetic field and the quadrupolar profile of electric field reveal that the eigenmode of a point defect in the surface-wave band-gap crystal is a localized magnetic toroidal mode and an electric quadrupole mode [36–38] with fourfold rotational symmetry.

Then, we simulate the magnetic and electric field distributions of a line-defect waveguide with a sharp corner, as shown in Figs. 5(b) and 5(e). We choose the frequency of 13.09 GHz for illustration in order to make the phase difference between fields of neighboring shortened rods exactly equal to $\pi/2$, such that when the magnetic and electric fields are maximum around one shortened rod, they are zero around the neighboring shortened rod. Thus, the overlap of fields between neighboring shortened rods will not obscure the mode profile of each shortened rod to be observed. It can be seen that even in an array of closely positioned shortened rods, the magnetic toroidal mode and the electric quadrupole mode of each shortened rod still maintain their mode profiles with fourfold rotational symmetry. This is in sharp contrast to typical plasmonic waveguides formed by an array of plasmonic resonators [50–51]. For typical coupled plasmonic resonators, only when their coupling strength is weak can each resonator maintain its mode profile [39,52–53]. Yet in a surface-wave band-gap crystal, the fourfold rotational symmetry of the mode profile around a shortened rod is maintained by the crystal symmetry rather than the coupling strength between neighboring shortened rods.

For comparison, we also plot the magnetic and electric field distributions of a domino-plasmon sharp bend, when all other rods in the surface-wave band-gap crystal are removed, as shown in Figs. 5(c) and 5(f). The frequency of 12.00 GHz is used to set the phase difference between neighboring rods equal to $\pi/2$. It can be observed that without the surrounding surface-wave band-gap crystal, the magnetic and the electric fields do not exhibit fourfold rotational symmetry.

The fourfold rotational symmetry of the mode profile is the key to realize near-perfect guidance around a sharp right angle. When propagating through the right angle, because of the presence of the preserved fourfold rotational symmetry, the near-field couplings between the rod at the corner of right-angle bend and its two immediate neighbors before and after the right-angle bend are the same. Surface electromagnetic waves can be thereby deceived that they are still propagating along a straight-line-defect waveguide without any corners. In order words, the translational symmetry from the viewpoint of wave propagation is preserved. This "translational symmetry" mechanism for highly efficient transmission through sharp corners originates from Yariv's CROW theory [39].

A particularly appealing feature of the CROW is the possibility of making lossless and reflectionless bends from symmetry considerations. If the individual resonator mode possesses an n-fold rotational symmetry, one can make a perfect $2\pi/n$ bend, since the coupling of the corner resonator to its two immediate neighbors is identical. The transmission coefficient through the bend is 100% throughout the entire CROW band. The line-defect waveguide in the surface-wave

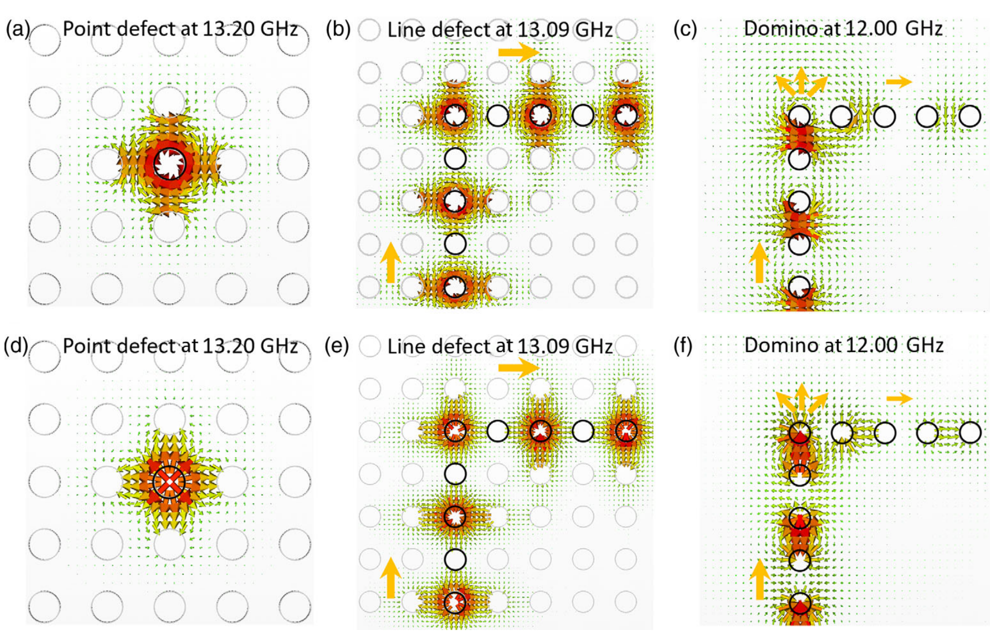

FIG. 5. Field distributions of a point defect, a line-defect sharp bend in the surface-wave band-gap crystal, and a domino-plasmon sharp bend without the surrounding surface-wave band-gap crystal. Magnetic (a)–(c) and electric (d)–(f) field distribution of (a),(d) an isolated point defect at 13.20 GHz, (b),(e) a line-defect sharp bend at 13.09 GHz, and (c),(f) a domino-plasmon sharp bend at 12.00 GHz in a transverse x-y plane at half height of the 5-mm-high metallic rods. Black circles represent the line defect with shortened rods. Gray circles represent the surrounding surface-wave band-gap crystal.

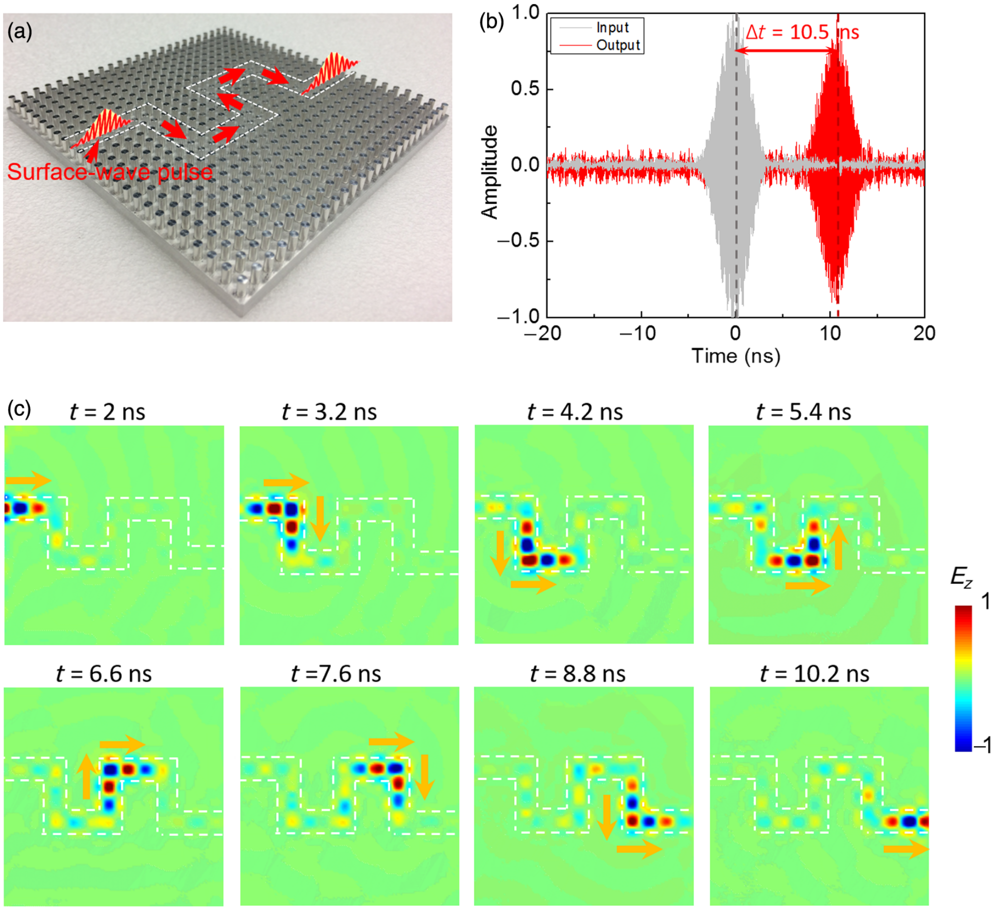

FIG. 6. Surface-wave pulse propagation around a tortuous line-defect waveguide. (a) Photograph of the tortuous line-defect waveguide. Inset shows the schematic of the pulse propagation. (b) Measured surface-wave pulse signals at the input and output of the tortuous waveguide. (c) Reconstructed surface-wave pulse propagation in the tortuous waveguide at different time frames.

photonic crystal is a type of CROW for surface waves; thus, the fourfold rotational symmetry of the point-defect cavity enables the highly efficient transmission through a right angle due to the inherent identical coupling of the corner rod to its two immediate neighbors at the right angle. On the other hand, without the fourfold rotational symmetry, serious scattering occurs at the right-angle sharp corner in a typical domino-plasmon waveguide [Figs. 5(c) and 5(f)] because of the dramatic momentum mismatch.

VI. TIME-DOMAIN SURFACE-WAVE PULSE PROPAGATION AROUND MULTIPLE SHARP RIGHT ANGLES

Because the height of the rods in the surface-wave band-gap crystal can be adjusted conveniently, it is feasible to form a tortuous path with multiple sharp right angles for routing surface-wave pulses.

In the following, we construct a tortuous line-defect waveguide with multiple sharp right angles [Fig. 6(a)] and launch the same surface-wave pulse (central frequency 13.4 GHz and bandwidth 0.8 GHz) to examine its performance. We measure the input pulse (gray line) and the output pulse (red line), as shown in Fig. 6(b). A time delay of 10.5 ns and only <10% amplitude decay can be observed after propagating through six sharp right angles in the surface-wave band-gap crystal. To gain deeper insight into the dynamic evolution of the pulse in the tortuous waveguide, we reconstruct the images of the pulse at different time frames, as shown in Fig. 6(c). It is clear that the pulse signal can smoothly propagate around all six sharp right angles without perceptible reflection or scattering, confirming the high transmission of surface waves through multiple sharp right angles along a complex path in the surface-wave band-gap crystal. Video S4 (see the video in the Supplemental Material [42]) shows more details about the dynamic evolution process of the pulse through the tortuous line-defect waveguide with multiple sharp right angles.

VII. CONCLUSIONS

In summary, by implementing a surface-wave band-gap crystal on a single metal surface, we provide a solution to routing surface-wave pulses around sharp right angles, as a step toward solving a long-lasting bottleneck in highly integrated subwavelength photonic circuits. We apply a time-resolved near-field imaging technique to reveal the dynamics of a surface-wave pulse in both space and time as the pulse propagates through multiple sharp right angles along an arbitrary path without perceptible scattering. The concept and method are general and can be directly applied to the terahertz and far-infrared frequency ranges to realize ultracompact terahertz and photonic circuits with high performance and high integration density.

ACKNOWLEDGMENTS

This work is sponsored by the NTU Start-Up Grants and Nanyang Research Grant (Young Investigator), Singapore Ministry of Education (MOE) under Grants No. MOE2015-T2-1-070, No. MOE2016-T3-1-006, No. MOE2015-T2-1-145, No. Tier 1 RG72/15, and No. Tier 1 RG91/17 (S), National Research Foundation-Competitive Research Programme (NRF-CRP) Grant No. NRF2015NRF-CRP002-008, and Young Thousand Talent Plan, China.

[1] H. Raether, *Surface Plasmons on Smooth and Rough Surfaces and on Gratings* (Springer-Verlag, New York, 1988).

[2] E. Ozbay, Plasmonics: Merging photonics and electronics at nanoscale dimensions, Science **311**, 189 (2006).

[3] S. I. Bozhevolnyi, V. S. Volkov, E. Devaux, J. Y. Laluet, and T. W. Ebbesen, Channel plasmon subwavelength waveguide components including interferometers and ring resonators, Nature (London) **440**, 508 (2006).

[4] J. B. Pendry, L. Martín-Moreno, and F. J. García Vidal, Mimicking surface plasmons with structured surfaces, Science **305**, 847 (2004).

[5] A. P. Hibbins, B. R. Evans, and J. R. Sambles, Experimental verification of designer surface plasmons, Science **308**, 670 (2005).

[6] C. R. Williams, S. R. Andrews, S. A. Maier, A. I. Fernández-Domínguez, L. Martín-Moreno, and F. J. García-Vidal, Highly confined guiding of terahertz surface plasmon polaritons on structured metal surfaces, Nat. Photonics **2**, 175 (2008).

[7] Q. Gan, Z. Fu, Y. J. Ding, and F. J. Bartoli, Ultrawide-Bandwidth Slow-Light System Based on THz Plasmonic Graded Metallic Grating Structures, Phys. Rev. Lett. **100**, 256803 (2008).

[8] D. Martin-Cano, M. L. Nesterov, A. I. Fernandez-Dominguez, F. J. García Vidal, L. Martin-Moreno, and E. Moreno, Domino plasmons for subwavelength terahertz circuitry, Opt. Express **18**, 754 (2010).

[9] N. F. Yu, Q. J. Wang, M. A. Kats, J. A. Fan, S. P. Khanna, L. H. Li, A. G. Davies, E. H. Linfield, and F. Capasso, Designer spoof surface plasmon structures collimate terahertz laser beams, Nat. Mater. **9**, 730 (2010).

[10] X. P. Shen, T. J. Cui, D. Martin-Cano, and F. J. García Vidal, Conformal surface plasmons propagating on ultrathin and flexible films, Proc. Natl. Acad. Sci. U.S.A. **110**, 40 (2013).

[11] A. Pors, E. Moreno, L. Martin-Moreno, J. B. Pendry, and F. J. García Vidal, Localized Spoof Plasmons Arise While Texturing Closed Surfaces, Phys. Rev. Lett. **108**, 223905 (2012).

[12] X. P. Shen and T. J. Cui, Ultrathin plasmonic metamaterial for spoof localized surface plasmons, Laser Photonics Rev. **8**, 137 (2014).

[13] Y. Yang, L. Jing, L. Shen, Z. Wang, B. Zheng, H. Wang, E. Li, N. Shen, T. Koschny, C. M. Soukoulis, and H. Chen, Hyperbolic spoof plasmonic metasurfaces, NPG Asia Mater. **9**, e428 (2017).

[14] Z. Wang, Y. Chong, J. D. Joannopoulos, and M. Soljačić, Observation of unidirectional backscattering-immune topological electromagnetic states, Nature (London) **461**, 772 (2009).

[15] L. Lu, J. D. Joannopoulos, and M. Soljačić, Topological photonics, Nat. Photonics **8**, 821 (2014).

[16] A. B. Khanikaev, S. H. Mousavi, W. K. Tse, M. Kargarian, A. H. MacDonald, and G. Shvets, Photonic topological insulators, Nat. Mater. **12**, 233 (2013).

[17] X. Cheng, C. Jouvaud, X. Ni, S. H. Mousavi, A. Z. Genack, and A. B. Khanikaev, Robust reconfigurable electromagnetic pathways within a photonic topological insulator, Nat. Mater. **15**, 542 (2016).

[18] W. J. Chen, Z. Q. Zhang, J. W. Dong, and C. T. Chan, Symmetry-protected transport in a pseudospin-polarized waveguide, Nat. Commun. **6**, 8183 (2015).

[19] S. Xu, H. Y. Xu, H. H. Gao, Y. Y. Jiang, F. X. Yu, J. D. Joannopoulos, M. Soljačić, H. S. Chen, H. D. Sun, and B. L. Zhang, Broadband surface-wave transformation cloak, Proc. Natl. Acad. Sci. U.S.A. **112**, 7635 (2015).

[20] M. L. M. Balistreri, H. Gersen, J. P. Korterik, L. Kuipers, and N. F. van Hulst, Tracking femtosecond laser pulses in space and time, Science **294**, 1080 (2001).

[21] R. J. P. Engelen, Y. Sugimoto, H. Gersen, N. Ikeda, K. Asakawa, and L. Kuipers, Ultrafast evolution of photonic eigenstates in k-space, Nat. Phys. **3**, 401 (2007).

[22] H. Gersen, T. J. Karle, R. J. P Engelen, W. Bogaerts, J. P. Korterik, N. F. van Hulst, T. F. Krauss, and L. Kuipers, Real-Space Observation of Ultraslow Light in Photonic Crystal Waveguides, Phys. Rev. Lett. **94**, 073903 (2005).

[23] M. Sandtke and L. Kuipers, Slow guided surface plasmons at telecom frequencies, Nat. Photonics **1**, 573 (2007).

[24] A. Kubo, N. Pontius, and H. Petek, Femtosecond microscopy of surface plasmon polariton wave packet evolution at the silver/vacuum interface, Nano Lett. **7**, 470 (2007).

[25] N. Rotenberg, M. Spasenovic, T. L. Krijger, B. Feber, F. J. García de Abajo, and L. Kuipers, Plasmon Scattering from Single Subwavelength Holes, Phys. Rev. Lett. **108**, 127402 (2012).

[26] C. Lemke, C. Schneider, T. Leißner, D. Bayer, J. W. Radke, A. Fischer, P. Melchior, A. B. Evlyukhin, B. N. Chichkov, C. Reinhardt, M. Bauer, and M. Aeschlimann, Spatiotemporal characterization of SPP pulse propagation in two-dimensional plasmonic focusing devices, Nano Lett. **13**, 1053 (2013).

[27] Y. Gong, A. G. Joly, D. Hu, P. Z. El-Khoury, and W. P. Hess, Ultrafast imaging of surface plasmons propagating on a gold surface, Nano Lett. **15**, 3472 (2015).

[28] Y. Nishiyama, K. Imura, and H. Okamoto, Observation of plasmon wave packet motions via femtosecond time-resolved near-field imaging techniques, Nano Lett. **15**, 7657 (2015).

[29] Z. Gao and B. L. Zhang, Surface-wave pulse routing around sharp corners, arXiv:1604.06872v2.

[30] N. Kaina, A. Causier, Y. Bourlier, M. Fink, T. Berthelot, and G. Lerosey, Slow waves in locally resonant metamaterials line defect waveguides, Sci. Rep. **7**, 15105 (2017).

[31] S. C. Kitson, W. L. Barnes, and J. R. Sambles, Full Photonic Band Gap for Surface Modes in the Visible, Phys. Rev. Lett. **77**, 2670 (1996).

[32] S. I. Bozhevolnyi, J. Erland, K. Leosson, P. M. W. Skovgaard, and J. M. Hvam, Waveguiding in Surface Plasmon Polariton Band Gap Structures, Phys. Rev. Lett. **86**, 3008 (2001).

[33] J. D. Joannopoulos, R. D. Meade, and J. N. Winn, *Photonic Crystals: Molding the Flow of Light* (Princeton University Press, Princeton, NJ, 2008).

[34] A. Mekis, J. C. Chen, I. Kurland, S. Fan, P. R. Villeneuve, and J. D. Joannopoulos, High Transmission through Sharp Bends in Photonic Crystal Waveguides, Phys. Rev. Lett. **77**, 3787 (1996).

[35] S. Y. Lin, E. Chow, V. Hietala, P. R. Villeneuve, and J. D. Joannopoulos, Experimental demonstration of guiding and bending of electromagnetic waves in a photonic crystal, Science **282**, 274 (1998).

[36] N. Papasimakis, V. A. Fedotov, V. Savinov, T. A. Raybould, and N. I. Zheludev, Electromagnetic toroidal excitations in matter and free space, Nat. Mater. **15**, 263 (2016).

[37] S. H. Kim, S. S. Oh, K. J. Kim, J. E. Kim, H. Y. Park, O. Hess, and C. S. Kee, Subwavelength localization and toroidal dipole moment of spoof surface plasmon polaritons, Phys. Rev. B **91**, 035116 (2015).

[38] Z. Gao, F. Gao, and B. L. Zhang, Guiding, bending, and splitting of coupled defect surface modes in a surface-wave photonic crystal, Appl. Phys. Lett. **108**, 041105 (2016).

[39] A. Yariv, Y. Xu, R. K. Lee, and A. Scherer, Coupled-resonator optical waveguide: A proposal and analysis, Opt. Lett. **24**, 711 (1999).

[40] A. E. Miroshnichenko, E. Andrey, and Y. S. Kivshar, Sharp bends in photonic crystal waveguides as nonlinear Fano resonators, Opt. Express **13**, 3969 (2005).

[41] A. Mekis, S. Fan, and J. D. Joannopoulos, Bound states in photonic crystal waveguides and waveguide bends, Phys. Rev. B **58**, 4809 (1998).

[42] See Supplemental Material at http://link.aps.org/supplemental/10.1103/PhysRevApplied.9.044019 for additional experimental and numerical calculation results, as well as the reconstructed videos for the surface-wave pulse routing.

[43] W. S. Zhao, O. M. Eldaiki, R. Yang, and Z. L. Lu, Deep subwavelength waveguiding and focusing based on designer surface plasmons, Opt. Express **18**, 21498 (2010).

[44] D. Martin-Cano, O. Quevedo-Teruel, E. Moreno, L. Martin-Moreno, and F. J. García Vidal, Waveguided spoof surface plasmons with deep-subwavelength lateral confinement, Opt. Lett. **36**, 4635 (2011).

[45] E. M. G. Brock, E. Hendry, and A. P. Hibbins, Appl. Phys. Lett. **99**, 051108 (2011).

[46] Y. G. Ma, L. Lan, S. M. Zhong, and C. K. Ong, Experimental demonstration of subwavelength domino plasmon devices for compact high-frequency circuit, Opt. Express **19**, 21189 (2011).

[47] F. Gao, Z. Gao, X. Shi, Z. Yang, X. Lin, J. D. Joannopoulos, M. Soljačić, H. Chen, L. Lu, Y. Chong, and B. Zhang, Probing topological protection using a designer surface plasmon structure, Nat. Commun. **7**, 11619 (2016).

[48] W. Tang, H. Zhang, J. Liu, J. Xu, and T. J. Cui, Reduction of radiation loss at small-radius bend using spoof surface plasmon polariton transmission line, Sci. Rep. **7**, 41077 (2017).

[49] H. Zhang, T. J. Cui, Q. Zhang, Y. Fan, and X. Fu, Breaking the challenge of signal integrity using time-domain spoof surface plasmon polaritons, ACS Photonics **2**, 1333 (2015).

[50] S. Maier, P. Kik, H. Atwater, S. Meltzer, E. Harel, B. Koel, and A. Requicha, Local detection of electromagnetic energy transport below the diffraction limit in metal nanoparticle plasmon waveguides, Nat. Mater. **2**, 229 (2003).

[51] P. Qin, Y. Yang, M. Y. Musa, B. Zheng, Z. Wang, R. Hao, W. Yin, H. Chen, and E. Li, Toroidal localized spoof plasmons on compact metadisks, Adv. Sci. **4**, 1700487 (2017).

[52] X. Dai, X. Li, Y. Li, and P. A. Hu, Maximum efficiency tracking for wireless power transfer systems with dynamic coupling coefficient estimation, IEEE Transactions on Power Electronics **33**, 5005 (2017).

[53] X. Dai, X. Li, Y. Li, and P. A. Hu, Impedance matching range extension method for maximum power transfer tracking in IPT system, IEEE transactions on power electronics **33**, 4419 (2017).